Article

Magnetic soft millirobot with simultaneous locomotion and sensing capability

Check for updates

Weihong Zeng[1,6], Xinrui Ding[2,6], Yuan Jin[3,6], Bin Liu[4], Runhao Zeng[5] ✉, Feng Gong[1], Yan Lou[1], Lelun Jiang[4] ✉ & Hui Li[1] ✉

Soft millirobot has attracted significant attention and demonstrated tremendous potential in human-robot interactions and safety inspections. Locomotion and perception are two crucial features for achieving effective gait and practical applications of robots. Inspired by nature, this research reports a magnetic soft millirobot that integrates locomotion and sensing capacities simultaneously. Microconical matrix with rich and regular surface morphologies are constructed directly inside the millirobot as both multilegged and triboelectric-enhanced sensing structures via cooperation of jet printing and magnetization-induction method with high-speed and high-precision. The robot can both recognize its current body state across various application scenarios and identify terrains through a machine learning strategy. Our work presents a customizable approach for smart millirobots to perform tasks in nonmagnetic structured environments and provides embedded sensing capability for next-generation soft robots.

Nature has long been the source of human inspiration for the development of innovative, complex, and valuable robots[1]. As a significant branch of robotics science and engineering, soft robots are made from compliant and flexible materials, garnering considerable attentions in recent years[2]. Owing to the advantages of inherent softness, excellent environmental adaptability, and multiple degrees of freedom, soft robots have demonstrated significant applications across various fields, such as soft manipulators and actuators[3,4], safe human-machine interaction[5], minimally invasive surgery[6], biomedical engineering[7,8] and pipeline inspection[9,10]. To date, researchers have developed numerous soft robots with diverse locomotion control modes[11]. Notably, the design of micro/millimeter-scale robots drawn inspiration from the movements of fish, turtles, geckos, insects and other creatures, to achieve a series of biological actions and navigate unknown environment[12,13].

Generally, the actuation methods for soft robots can be provided through various methods, including pressure[14,15], heat[16,17], light[18], electric field[12,19], magnetic field[20,21], etc. Among these response methods, magnetic actuation shows great potentiality due to many unique advantages, such as non-contact and fully controllability. Consequently, magnetic soft robots are particularly well-suited for performing non-invasive safety operations inside narrow areas[22,23]. Under electromagnetic actuation system or permanent magnetic actuation system, the fabricated robots can achieve the required locomotion facilely[24,25]. To enhance locomotion efficiency of magnetic soft robots, multi-legged structures, commonly found in living animals, are employed to help both lift the body off ground and reduce friction[26]. Common fabrication methods for legs include spin coating and templating assisted by magnetic field[27–29]. However, these soft legs usually distributed randomly and were weak for body supporting and extra-load bearing[30]. To achieve a consistent and uniform morphology for the legs, template fabrication method are frequently chosen, where the mold should be prepared accurately in advance[31]. Therefore, there remains low-cost and convenient approaches to fabricate the uniform multi-legged structure for magnetic soft robots.

Moreover, current progress about magnetic robot is mainly concerned with structure design and locomotion actuation, as can be seen in Supplementary Table 1. Nevertheless, accurate control of the motion state is challenging, making sensing capacity crucial for millirobot, especially for autonomous navigation in confined and enclosed environments[32,33], as well as for traversing unknow terrains during delivery and inspection tasks[34,35]. Moreover, due to the flexibility requirements of soft robots, sensors should

[1]Guangdong Provincial Key Laboratory of Micro/Nano Optomechatronics Engineering, College of Mechatronics and Control Engineering, Shenzhen University, Shenzhen, China. [2]School of Mechanical and Automotive Engineering, South China University of Technology, Guangzhou, China. [3]School of Mechanical Engineering and Mechanics, Ningbo University, Ningbo, China. [4]School of Biomedical Engineering, Shenzhen Campus of Sun Yat-sen University, Shenzhen, China. [5]Artificial Intelligence Research Institute, Shenzhen MSU-BIT University, Shenzhen, China. [6]These authors contributed equally: Weihong Zeng, Xinrui Ding, Yuan Jin. ✉e-mail: zengrh@smbu.edu.cn; jianglel@mail.sysu.edu.cn; huili@szu.edu.cn

also possess high flexibility and repeatability[36]. Therefore, it is still significant challenging to integrate additional sensor into the small robot body for proprioception and even exteroception.

In this work, we introduced an inchworm-inspired millirobot that integrates locomotion and sensing capacities to address the aforementioned challenges. This millirobot features with multilayered soft functional structures, enabling it to move and sense through coupling of magnetic effects and triboelectric sensing effects. To fabricate the millirobot, a cooperative jet printing and magnetization-induction (CJM) method is developed which offers advantages such as high precision, high efficiency and excellent uniformity. A three-dimensional microconical matrix with rich surface morphology is constructed inside the millirobot to strengthen both motion and sensing performance. Under the trigger of an external magnetic field, the soft millirobot can achieve bidirectional, load-bearing, and narrow space passing locomotion while simultaneously generating corresponding electrical signals. By analyzing data collected by the onboard sensor, the millirobot is demonstrated to recognize its current body state in application scenarios with structured environments and realize the exteroceptive sensing capabilities with the assistance of a novel machine learning strategy.

Results
Design and fabrication of magnetic soft millirobot
The unique locomotion mechanism of inchworm has inspired the structural design of soft bodied robots. Based on the anchor motion crawling principle, the mobility of inchworm has strong interactions with uncertain and complex environments[37]. Currently, enhancing the actuation performance and autonomous motion ability of the inchworm-inspired robot remains a significant challenging[38]. In this study, we developed a soft robot to achieve crawling locomotion and sensing ability to an inchworm through magnetic actuation system. As shown in Fig. 1a, the magnetic soft millirobot primarily consists of two functional components, including the bottom driven module and the upper sensing module. The driven module includes a driven layer and a multi-legged microconical matrix, while the sensing module comprises a dielectric charging layer formed by another microconical matrix

sandwiched between two electrodes. The entire millirobot is fabricated based on CJM, while detailed fabrication process is shown in Supplementary Fig. 1 and thoroughly stated in Methods section. Briefly, printable magnetic ink is prepared and jet printed onto a PVC substrate to form the driven layer. After curing, the ink is jet printed to create the matrix on the driven layer. To induce the formation of multi-legged structures on the driven layer, an external magnetic field is timely applied on the matrix before solidification process. Then, two driven layers are magnetized in opposite directions and connected with each other by jet printing. A polyurethane (PU) film and an electrode are sequentially covered on the driven layer. Finally, the micro-conical matrix is constructed on the polyethylene glycol terephthalate (PET) film with an electrode via CJM, serving as the enhanced dielectric charging layer.

Figure 1b compares the typical flat and bending locomotion behaviors between an inchworm and our millirobot. A prototype of the millirobot is illustrated alongside a Chinese 10 yuan coin, with the entire robot measuring $20 \times 8 \times 2.5 \, \text{mm}^3$. Figure 1c shows the photograph and 3D surface profilometer results of the driven module with 5×5 microconical matrix. The matrix exhibits properties of flexibility and stretchability, with each microcone uniformly shaped and colored black. As shown in Fig. 1d, the millirobot can deform into an arch shape under the influence of a magnetic field, facilitating contact between the positive electrode and dielectric charging layer in the sensing module. Due to the coupling effect of contact electrification and electrostatic induction, the sensor can generate electrons along the external circuit[39]. This signal demonstrates the promising potential of the sensing system for proprioception and exteroception.

Figure 2a shows fabrication process of the microconical matrix based on CJM. The fabrication begins by mixing silicone rubber with magnetic materials at room temperature to prepare the ink. This ink is then jet printed using a drop-on-demand material jetting system, specifically designed for high-viscosity material. Under the action of a piezoelectric-pneumatic material jetting actuator, droplet are ejected through the orifice in the nozzle tip and precisely deposit onto substrate, controlled by the driven voltage. Supplementary Fig. 2 provides the corresponding voltage parameters used in the drop-on-demand material jetting system in the experiment. By
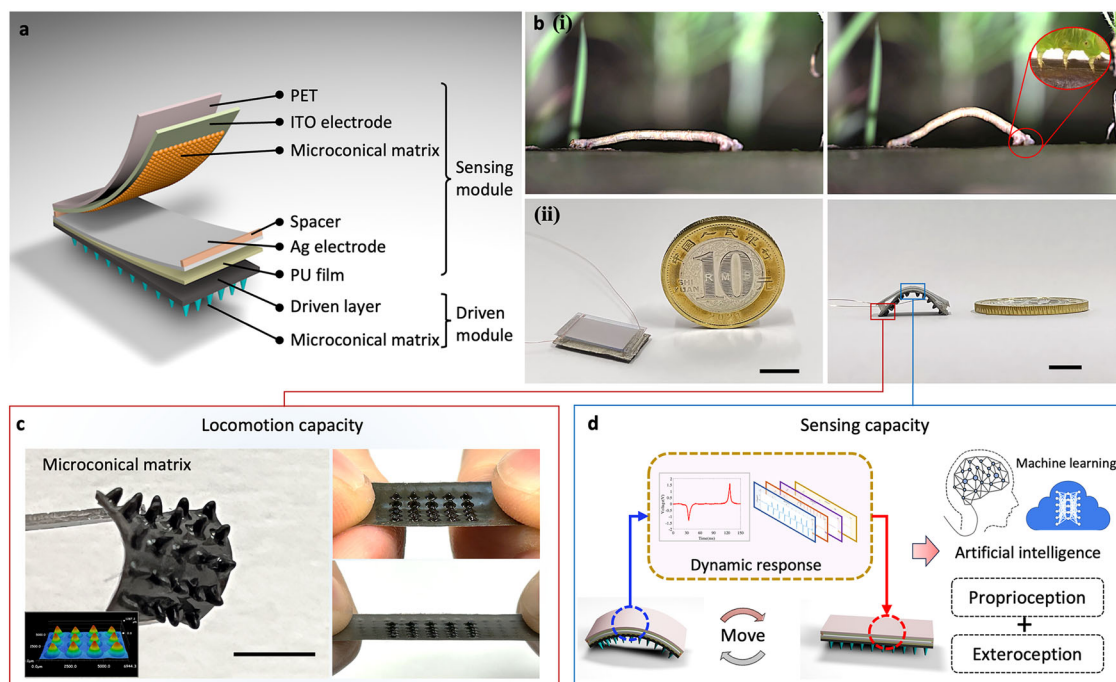
Fig. 1 | Overview of magnetic soft millirobot. a Schematic diagram of the milli-robot. **b** (i) Typical locomotion behavior of the inchworm in flat and bending states, (ii) locomotion behaviors of the millirobot. Optical images showing the size of the millirobot, alongside a Chinese 10 yuan coin. **c** Microconical matrix in millirobot to enhance locomotion capacity. Inset shows 3D surface profilometer result of microconical matrix. Flexibility and stretchability of the driven module. **d** Sensing functionality of millirobot to integrate with machine learning strategy. (Scale bar: 10 mm).
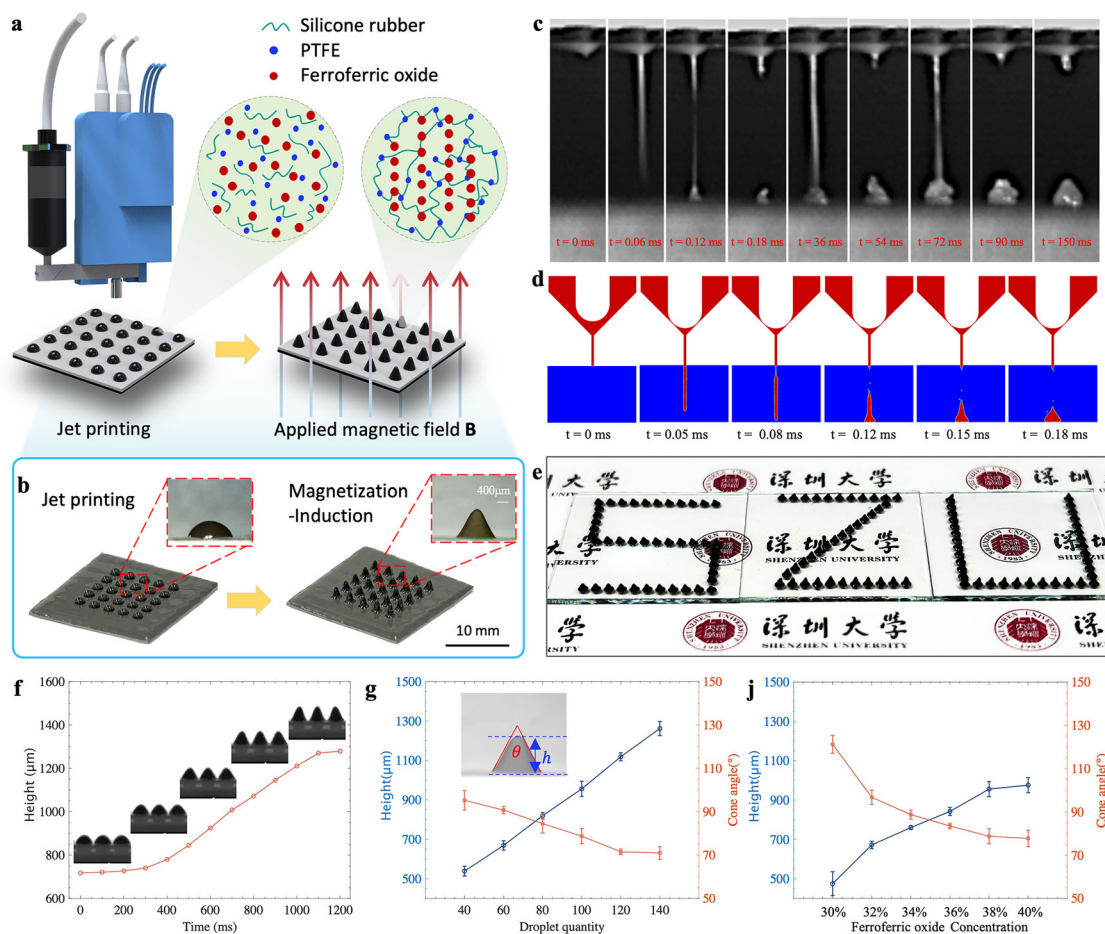
Fig. 2 | Fabrication and characterization of the microconical matrix. a Schematic illustrations of the cooperation of jet printing and magnetization-induction method, forming process of microconical matrix and magnetized behavior in the ink. **b** Photographs of microconical matrix after jet printing and magnetization-induction processes, respectively. Insets show the shapes of microconical matrix. **c** Image sequence of jet printing process under high speed camera. **d** Simulation results of jet printing process. **e** Optical photographs of the printed patterns "SZU" via cooperation of jet printing and magnetization-induction. **f** Dynamic curve for generation process of the microcone. **g** The influence of the droplet quantity on shape parameters of microconical matrix. **h** The influence of ferroferric oxide concentration on shape parameters of microconical matrix.

controlling various fabrication parameters, such as ink properties, droplet spacing, and droplet quantality, the functional layers for the millirobot can be accurately produced. Subsequently, when the parallel magnetic field is applied to the deposited droplet, their shape rapidly and uniformly transforms from hemispherical to microconical. Figure 2b shows the photographs of microconical matrix after jet printing and magnetization-induction, respectively.

Figure 2c shows the detailed image sequences of several pulses in jet printing process for microconical structures. When the piezoelectric stack inside the printing head is powered off, a high pressure can be instantaneously provided by the tappet, forcing the ink to be ejected through the nozzle orifice. Because of the inertia force and high viscosity of the ink, the ejected droplet is prolonged, creating a continuous liquid column between the printing head and substrate in one pulse ($t = 0–0.18$ ms). As the volume of ejected material increases, droplet accumulate above the substrate generally. Supplementary Movie 1 shows the detailed visualization of the jet printing process. This phenomenon is further demonstrated through the simulation results, as shown in Fig. 2d. The fluid velocity and pressure distribution during jet printing are shown in Supplementary Fig. 3. As the tappet moved down, the fluid velocity gradually increases. When the tappet strikes the nozzle, the velocity suddenly decreases to be zero, causing the extruded liquid to break off correspondingly. A more detailed analysis of the simulation is shown in Supplementary Note.1. Furthermore, CJM can be used to print freeform paths, showcasing its versatility in individual design

capacities. An optical photograph of the printed patterns "SZU" via CJM is shown in Fig. 2e.

To verify the effect of magnetization-induction, a high speed camera is also employed to capture the generation process of the microconical matrix, as shown in Supplementary Movie 2. The dynamic evolutions show that once parallel magnetic field is applied, the microcones flow upwards under the strengthening magnetic field, inducing an increase in height. The corresponding dynamic curve for the generation process of the microcone is presented in Fig. 2f. Initially, in unswollen condition, the height of the microcone is approximately 720 μm. Upon application of the magnetic field, the height increases to about 1280 μm and reaches a saturated-swollen condition. The possible reason for this behavior may be that initially, the magnetic magnetic-particles are dispersed randomly within the curable polymer fluid. Once the magnetic fluid is applied, adjacent particles align to form chains due to the magnetic interaction and aggregate into networks, driving the viscous fluid to grow upwards[40] (Supplementary Fig. 4). Additionally, the bottom diameter of the microcone does not present evident changes due to the adhesive force between substrate and droplet.

Figure 2g shows the influence of the droplet quantity on the shape parameters of microconical matrix. As expected, when the droplet quantity increases gradually, there is a greater availability of freely flowing material. Thus, the height of the microcone can reach a relatively larger level, while the apex angle gradually decreases. Figure 2h shows the effect of ferroferric
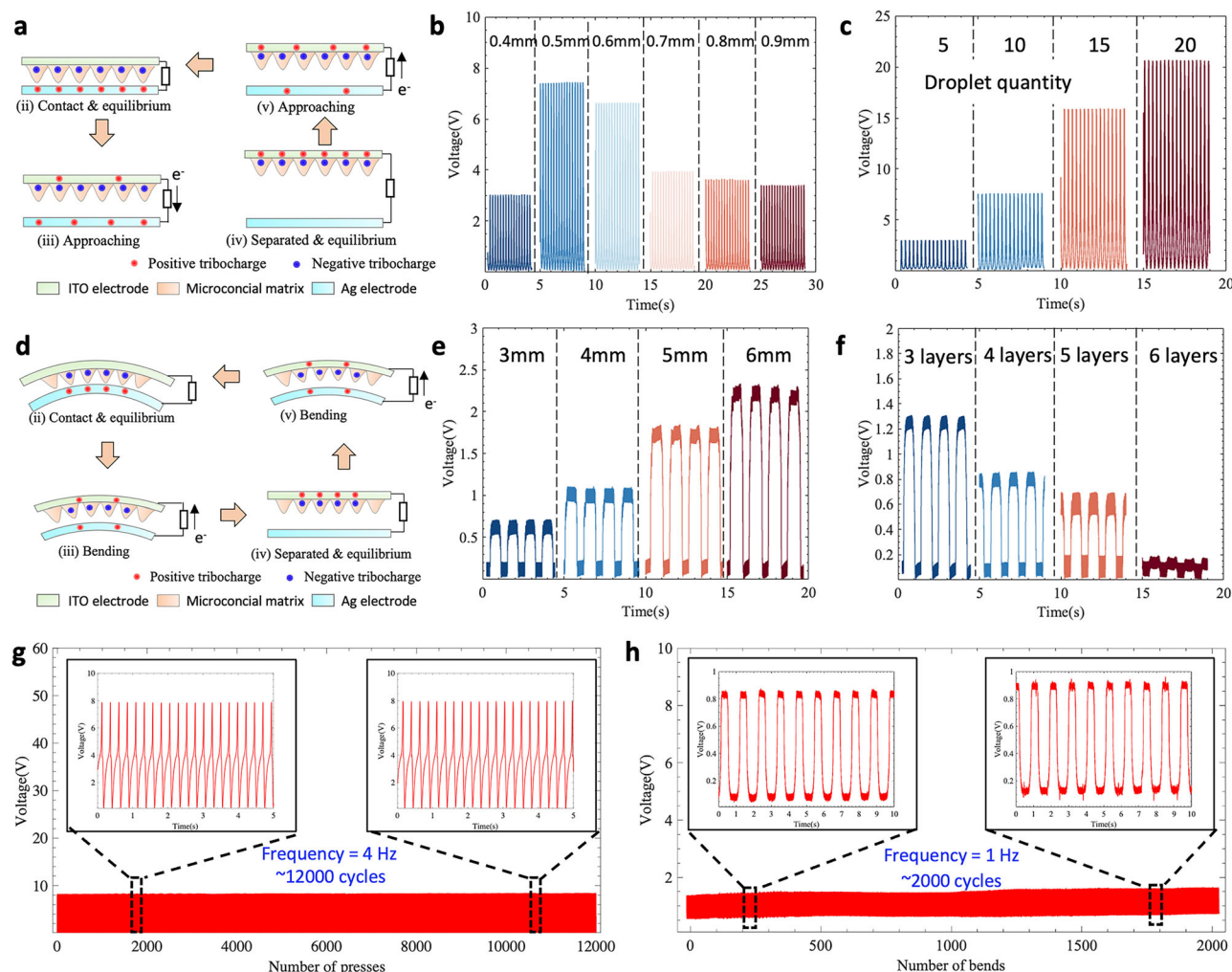
Fig. 3 | Output performance of sensing module in contact force. a Schematic illustration of the working principle at vertical contact-separation mode. **b** Output voltage of the TENG with various electrode size at 4 Hz frequency and at 5 N external force. **c** Influence of the droplet spacing for output voltage. Output performance of sensing module in bending test. **d** Schematic illustration of the working principle at bending mode. **e** Output voltage of the sensing module with various droplet space. **f** Output voltage of the TENG with various spacer thickness. **g** Stability measurement of sensing module under continuous compressive force for 12,000 cycles. Inset: partially enlarged view of the curve. **h** Stability measurement of sensing module under continuous bending force for 2000 cycles. Inset: partially enlarged view of the curve.

oxide concentration on the shape parameters. As with the increase of the concentration from 30% to 40%, the height also shows a significant upward trend, and the apex angle decrease accordingly. Furthermore, when droplet quantity increases, the weight of the microconical matrix raises linearly, as shown in Supplementary Fig. 5. Mechanical properties are also important for the millirobot. Supplementary Fig. 6 illustrates the tensile strength test of magnetic ink. As with the rise of the tensile strain, the stress follows a similar trend to that of silicone rubber. Supplementary Fig. 7 shows the durability of the microconical matrix. It is noted that microconical matrix is continuously compressed for 2000 cycles, while the applying force is controlled at 30 N. During the force loading period, the shape parameters are measured, which have no evident difference.

Electrical characteristics of the sensing module

Regarding to the sensing capacity of the millirobot, the sensing module was constructed based on the coupling effect of triboelectrification and electrostatic. This design leverages several key advantages, including material compatibility, self-powered operation, and light weight construction. The fundamental electric properties of the sensor are measured under two different modes in this study. Figure 3a shows the working principle of the sensing module under vertical contact-separation mode. Ag layer is used as

the positive electrode[41]. ITO layer is used as the negative electrode, and microconical matrix constructed on ITO is employed as the dielectric charging layer. Due to the vertical force, the positive electrode and microconical matrix can be contacted and separated in sequence, inducing the electron flow through an external circuit. This process allows for energy harvest and analyzing electric signal to achieve proprioception for the millirobot. The output performance of sensing module can be affected by several factors. As shown in Fig. 3b, open circuit voltages are measured under a 5 N cycle compressive force at a frequency of 4 Hz, with adjustable droplet spacing. The output voltage of the 0.5 mm droplet spacing is higher than others, and the value can reach 7.92 V appropriately. This increased voltage can be attributed to the greater number of microns constructed on the surface of the negative electrode layer, enhancing the specific area during compressing. With the rise of the droplet spacing, the microcones gradually separate, causing the corresponded voltages to decrease and tend to be the same gradually[42]. Additionally, it is interesting to find that when the space is 0.4 mm, the open-circuit voltage is merely 3.02 V, relatively lower than other parameters. This phenomenon may be attributed to the following two reasons. Firstly, the jet printed negative layer is close to be flat for the smaller droplet spacing, reducing the distance between the two electrodes. Secondly, the sample with 0.4 mm droplet spacing has comparatively excessive

material. During the compression process, the vibrational energy is absorbed by the deformation of the negative layer, so the tribocharges generated by the friction energy decrease correspondingly, resulting in the reduction of the output energy[43].

Droplet quantity is an important factor for the output performance of millirobot. As shown in Fig. 3c, output voltages are measured under 5 N external force and 4 Hz frequency. The more the droplets used, the higher the achievable output voltage[42]. Specifically, the sensing module with 20 droplets has the highest output voltage of about 25 V. The reason can be explained as follows. Firstly, the gap between each two droplets is filled with the negative material, enlarging the specific area during compression. Secondly, even though more droplets can form larger volume of microcone in comparison, the shape of cone is retained, thereby forcing the elastomer to undergo more deformation. However, the weight of millirobot should also be taken into consideration. Supplementary Fig. 8 shows the effect of electrode size for output voltage. As expected, the output voltage shows an upward trend, obviously as with the rise of the electrode size. This is reasonable because when the electrode size increases, the friction charges on the surface also increase, inducing higher output voltage[44].

Moreover, considering the structural deformation during the millirobot locomotion, the basic electric properties are also measured under bending mode in this study. Figure 3d illustrates the schematic diagram for the working principle of the sensing module in bending condition. For the reason that the strain of various films are different, Ag layer contacts with microconcial matrix under bending force. To investigate in the bending amplitude, Fig. 3e shows the effect of offset distance on output performance at the frequency of 1 Hz. With the applied offset distance varying from 3 to 6 mm, output voltage increases accordingly. Specifically, when the offset distance is 6 mm, the output voltage rises to 2.4 V, which is 3.4 times higher than that of the 3 mm distance. The corresponding optical images are presented in Supplementary Fig. 9, showing the lower positive electrode being forced to bend and contact with the upper one. As the offset distance decreases gradually, the increased amount of transferred charges can induce larger output voltages.

For the reason that the droplet density would introduce resistance for the bending deformation, the effect of droplet spacing is also taken into consideration, as can be seen in Supplementary Fig. 10. The corresponded open-circuit voltages are measured at the frequency of 1 Hz in bending mode. As expected, more microcones can contact with the positive electrode during deformation, so the lower droplet space can yield the higher voltage, similar with the vertical contact-separation mode. Another critical factor influencing output performance is the distance between the two electrodes. Spacer thickness is used to adjust the distance in this study, as shown in Supplementary Fig. 11. Figure 3f shows the output voltage for different spacer thickness. Under the same offset distance, output voltage decreases from 1.3 to 0.2 V, when the spacer layer rises from 3 to 6 layers. This phenomenon can be attributed to the fact that when the offset level is constant, the deformation of the base layer remains consistent. Therefore, a smaller spacer thickness can yield larger contact area between electrodes, leading to higher output voltages.

The durability and stability of the sensing module are evaluated in this study. Figure 3g shows the output voltage over a long-term durability test. The sensor is operated continuously for 12000 cycles without delay at 4 Hz frequency. It is found that the output voltage maintains stable during the repetitive test. The inset shows a detailed curve of output voltage changes in 5 s. Moreover, for the reason that the sensing module is composed of multilayers made with different materials, the reliability and stability should be guaranteed in bending deformation. We measure the output voltage of sensing module under bending force, as shown in Fig. 3h. The peak of the output voltage also maintains almost unchanged after 2000 cycles at 1 Hz. The sensitivity (S) of the sensing module under contact-separation mode is shown in Supplementary Fig. 12. Sensitivity is defined as $S = (d\Delta V/V_S)/dP$, where ΔV is the relative change of the voltage, V_S is the saturated voltage, and P is the applied pressure. The results show that the relationship between voltage and pressure remains nearly linear with two distinct slopes across two regions, and it is more sensitive in low-pressure state.

Dynamic locomotion and sensing behavior

Figure 4a shows dynamic locomotion comparisons between an inchworm and a prototype millirobot. The crawling locomotion of the designed millirobot exhibits a wavelike path and is achieved through a push-and-pull motion process. An acrylic sheet with 6 mm in thickness serves as the substrate for robot movement. A permanent magnet provides the dynamic magnetic field, which is driven by a three-axis motion platform (Supplementary Fig. 13). As shown in Supplementary Fig. 14, when the movement of the permanent magnet is regulated to follow in an "O" trajectory in X-Y plane, the distance and angle between the magnet and the driven module change regularly, inducing deformation in the millirobot. Initially, with the permanent magnet positioned underneath, no significant deformation is obtained in the robot. As the permanent magnet moves towards the soft robot from the front, the millirobot begins to bend and forms an arch structure under the magnetic torque gradient force, pulling its body forward. As the permanent magnet gradually moves back, the arch structure flattens and restores to the initial state. Consequently, with periodic movement of permanent magnet, the millirobot can move forward step by step. The dynamic motion of the millirobot is shown in Supplementary Movie 3. The corresponding signals can be generated through the sensing module at bending mode (Supplementary Fig. 15). Moreover, the crawling direction can be altered by controlling direction of "O" trajectory, thereby achieving a continuous bidirectional crawling locomotion, as shown in Supplementary Movie 4. Figure 4b shows the experimental results of the lateral displacement (blue line) and vertical displacement (red line) of the prototype robot under a magnetic field strength of 100 mT and frequency of 1 Hz. The lateral/vertical displacement is defined as the lateral/vertical movement of the centroid on the driven layer relative to its original position[34]. It is found that the lateral displacement exhibits the liner variation, while the vertical presents the periodic wavelike pattern. The millirobot moves at the average speed of 1.4 mm/s.

During the millirobot locomotion process, the electric output can be acquired via the sensor continuously, as can be seen in Supplementary Movie 5. As shown in Fig. 4c, the maximum voltage can reach ~0.3 V under 100 mT magnetic field strength and the 1 Hz frequency. The output performance of the millirobot is related to the deformation of the arch structure. We move the permanent magnet in vertical direction with different distances beneath the millirobot, as can be seen in Supplementary Fig. 16. The output voltage can reach 0.3 V with distance of 6 mm, 0.2 V higher than that of the 30 mm distance. The influence of frequency on output performance is also evaluated, as can be seen in Supplementary Fig. 17. Subsequently, we demonstrate an application of the millirobot by having it pass through a narrow confined space with the height of about 3 mm, which is 0.5 mm higher than the thickness of the robot. Figure 4d shows the electric output voltage during the passing process. Initially, the maximum output voltage is about 0.3 V. However, as the millirobot moves into the confined region, restricted space limits the deformation of the robot, leading to a decrease in output performance. The output voltage drops to around 0.15 V. Moreover, due to the existence of the leges, the millirobot can also walk through the swallow water environment (Supplementary Fig. 18). Meanwhile, load capacity of the millirobot is evaluated. Two polylactic acid (PLA) blocks with different weights are prepared for the experiment: 0.41 g (1.4 times heavier) and 1.55 g (5.2 times heavier), respectively. The robot can still move smoothly, as can be seen in Fig. 4e, f. The corresponding output voltages are shown in Supplementary Fig. 19. However, with a 1.6 g load, speed is reduced to about one-third of the original speed, as shown in Supplementary Movie 6.

Environment awareness of millirobot

To evaluate the dynamic moving behavior and environment perception capability of the designed millirobot, five different terrain surfaces are
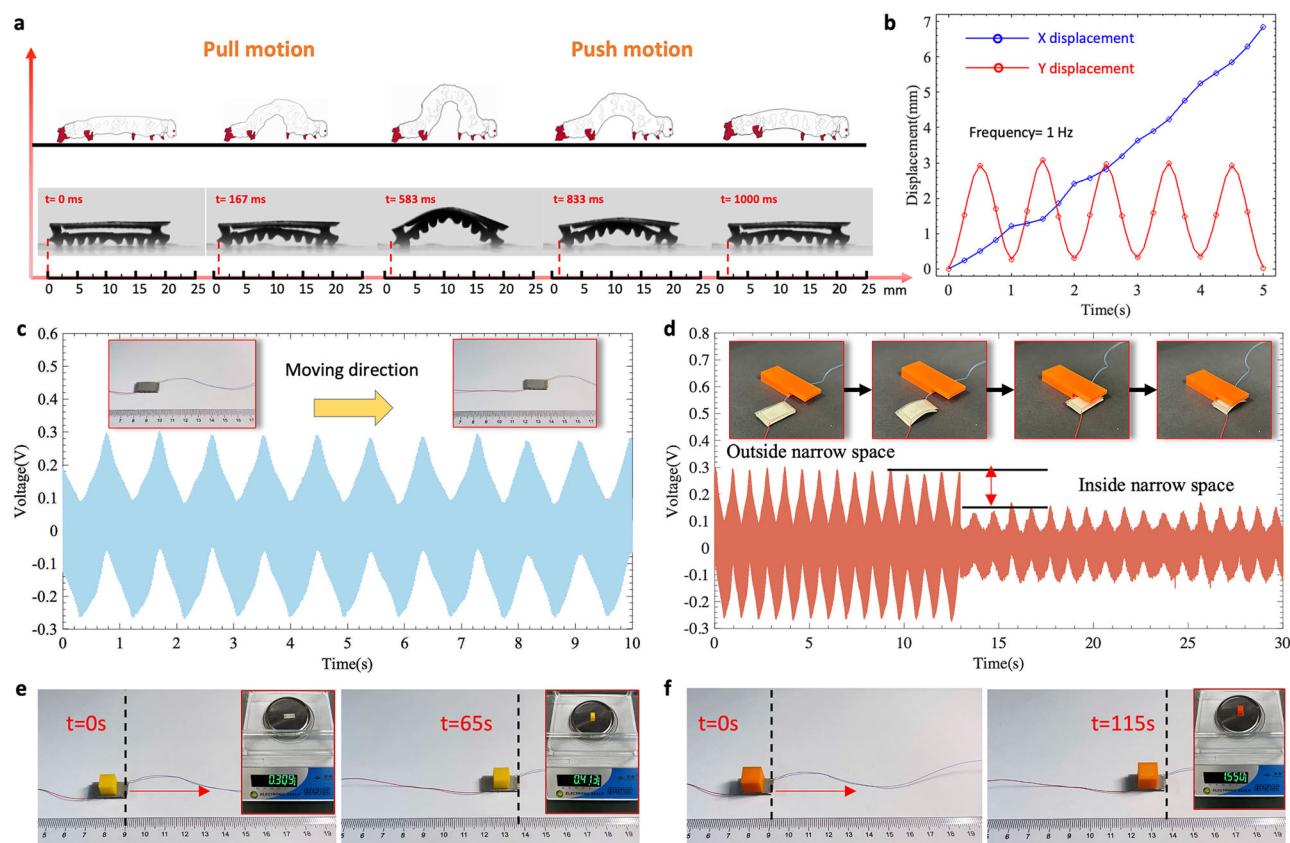
Fig. 4 | Millirobot locomotion and sensing capacities in motion. a Comparison of the wavelike paths showing the movements of the center point of an inchworm and a prototype millirobot. **b** Lateral displacement (Blue lines) and vertical displacement (Red lines) for center point of a prototype millirobot. **c** Corresponding output voltage during the robot locomotion, with the actuation frequency of 1 Hz. **d** Corresponding output voltage during the robot locomotion in confined space. A robot (0.31 g) carries two 3D printed objects, (**e**) 0.41 g and (**f**) 1.55 g, respectively.

selected and placed on the acrylic sheet for locomotion, including sandpaper, wood, plastic, printed PLA plate and napkin, as can be seen in Fig. 5a. Under conditions of a magnetic field strength 100 mT, distance between magnet and robot 6 mm and frequency 1 Hz, the output voltages for the above five terrain surfaces are presented in Fig. 5b, revealing differences in waveform expressions. The possible reason for the above results may be attributed to the surface morphology of each terrain, as can be seen from the SEM images in the inserts of Fig. 5a. Firstly, when the millirobot moves, the rear legs continuously slide on the ground. The roughness of the surface generates tiny vibration in the rear legs, thereby affecting the entire body of millirobot. These small body vibrations impact the stability of contact between the two electrodes in the sensing module, inducing different curve trends of output voltages across various terrain surface. Secondly, different terrain surfaces exhibit varying degrees of roughness, as can be seen in Supplementary Fig. 20. For surfaces with relatively lower roughness, such as plastic and PLA plate, there is less friction for the multi-legged structures during the millirobot locomotion. Consequently, the sensing module deforms into an arch shape with a smaller curvature radius, as can be seen in Supplementary Fig. 21. Thus, there would be greater force between Ag layer and microconical matrix in the sensing module, producing comparatively higher output voltage. In contrast, the other three terrain surfaces (sandpaper, wood, napkin) cause lower output voltages due to the larger surface roughness. The detailed locomotion processes can be found in Supplementary Movie 7.

For a comprehensive analysis, we divide the recorded data into training and testing sets, allocating 80% for training and 20% for testing, as shown in Fig. 5c. Each type of terrain provides 3000 time-series signal points, equivalent to a duration of 6 s. A sliding window method is employed for training sample selection, with a window size of 25 points (0.05 s) and a step

size of 15 points. The processed data, reorganized into two-dimensional time signals, are input to our proposed Temporal Perceiver Network (TPN). To visualize the learned features, we map the learned features to a low-dimensional space, as shown in Supplementary Fig. 22. Figure 5d shows a confusion matrix illustrating the network's performance in distinguishing among the five terrain types. TPN achieves an impressive overall accuracy of 96.7%. To verify the effectiveness of our algorithm, comparative analyses are conducted with two classic non-deep learning methods, including K-Nearest Neighbors & Dynamic Time Warping (KNN-DTW) and eXtreme gradient boosting (XGBoost). As indicated in Supplementary Fig. 23, the accuracies are 92.1% for KNN-DWT and 68.9% for XGBoost. More importantly, our algorithm exhibits superior computational efficiency. Therefore, the findings underscore the high accuracy and efficiency of our system in enabling environmental awareness for millirobots, showcasing its potential in terrain perception.

Discussion

In summary, inspired by nature, we have developed a magnetic millirobot with the ability to locomote and sense simultaneously in this study. Leveraging the core concept of additive manufacturing technology, the millirobot is composed of driven module and sensing module and fabricated by CJM in high-speed and high-precision. The multi-legged microconical matrix beneath the driven layer can effectively lift the body off the ground, providing adaptability to various environments. Meanwhile, the sensing capacity is achieved by triboelectric energy harvesting and enhanced through embedding a complex and regular microconical matrix within the sensing module. Under the trigger of the external magnetic field, our robot can achieve locomotion with realizing proprioceptive responses in application scenarios with nonmagnetic structured environments, such as nylon
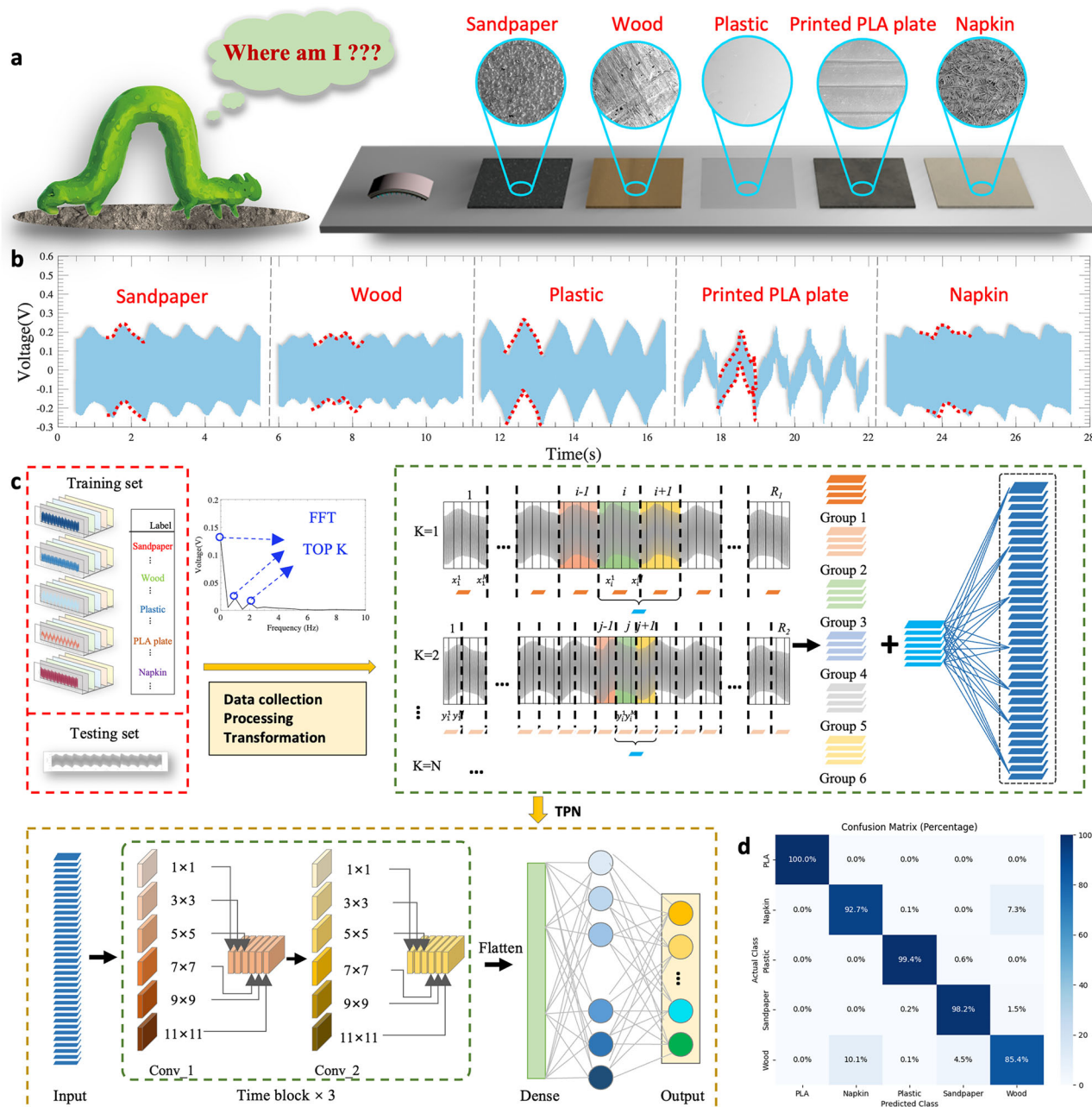
Fig. 5 | Dynamic moving behavior analysis and environment perception of millirobot crawling on various terrain surfaces. a Schematic of the millirobot crawling over various terrains. The enlarged views are SEM images of different terrain surfaces. **b** Signal responses when the millirobot robot crawling on sandpaper, wood, plastic, printed PLA plate and napkin, respectively. **c** Flow diagram of the machine learning process. Schematics of the process and parameters for data collection and processing, and convolutional neural network structure construction. **d** The confusion map for machine learning outcome of 5 various objects. Mixed recognition of all the aforementioned environments, with an overall accuracy of 96.7%.

and plastic pipelines. Moreover, the robot can utilize machine learning-based analysis methods to recognize various terrains and demonstrate exteroception. Hence, we hope the proposed soft magnetic millirobot and its related fabrication methods pave the way to shorten individual design cycle and offer smart and multifunctional sensing capacity for next-generation magnetic soft robots.

In the future, the research will focus on extending the application of millirobot into nonmagnetic pipeline inspection, which is a critical and challenging application in industrial settings. The compact size and advanced sensing capacity of the millirobot make it ideal for detect structural anomalies by analyzing terrain-specific voltage signatures. Additionally, its load capacity allows for integration of sensors to simultaneously monitor gas leaks. This dual functionality would enable real-time mapping and risk alert in pipelines. To realize this potential, the issues, such as wireless communication, dynamic 3D magnetic fields, long-term durability, and locomotion stability, should be investigated accordingly.

Methods
Material
To obtain the printable magnetic ink, ferroferric oxide with the size of 20 nm (Zhongye Co., China), NdFeB with the size 5 μm Xinnuode Co., China), nanosized PTFE particles (Zhonglian Plastic Chemical Co., China), and silicone rubber (Smooth-On Inc., USA) were mixed together via the

planetary mixer (AR-100, Thinky, Japan) for 5 min at 2000 rpm and vacuum deaeration for 5 min.

Fabrication of magnetic soft millirobot

The magnetic soft millirobot was composed of multilayered films. To create the driven layer, ink was jet-printed onto the polyvinyl chloride plate (PVC, Jiangwang Co., China). After curing, independent droplets were directly printed on the driven layer, where the shape of the droplet was hemispherical. Next, the sample was immediately placed under a parallel magnetic field before solidification, inducing the formation of the multi-legged microconical matrix for soft millirobot. The external magnetic field strength was 270 mT, and the direction was perpendicular to the substrate. To ensure the complete solidification of the microconical matrix, the exposure time in magnetic field was fixed at 60 s. After peeling off from the PVC plate, two whole driven layers were magnetized using a strong 3 T pulsed magnetic field using a magnetizer (M20-2040, Dongguan Haiteli Company, China). These two driven layers were connected together by silicone rubber via jet printing. Then, Ag film was coated on PU film via spray coating as the positive electrode. This PU film was subsequently pasted on the back of the driven module. ITO was coated onto a Polyethylene terephthalate substrate (PET, Jiangwang Co., China, 50 μm thickness) via magnetron sputtering as the negative electrode. Printable ink was jet printed on ITO as the dielectric charging layer, with printing parameters, such as droplet spacing, droplet quantity, and ink properties, carefully controlled to adjust the shape parameters of microconical matrix. Finally, two wires were attached to the two electrodes for electrical data collection. Silicone rubber was jet printed at two opposite ends of the electrodes as the spacer and covered the wire.

It should be noted that in order to maximize locomotion efficiency and sensing capability of the millirobot, the microconical matrix in driven layer and sensing layer are designed with distinct structural parameters. For the driven module, we aimed to mimic the biological leg morphology, where the length of animal legs was normally 1–2 times larger than their foot-to-foot spacing typically[28]. To optimize locomotion performance, we chose a radio of 1:1. The droplet spacing was controlled to be 1300 μm, and the height was 1280 μm. For the sensing module, the output performance could be enhanced by increasing the specific area. Therefore, a denser microconical matrix was employed with droplet spacing of 500 μm and height of 700 μm. The detailed fabrication parameters for these two microconical matrixes were shown in Supplementary Table 2. The corresponding ink viscosities were shown in Supplementary Fig. 24.

Moreover, during jet printing process, a driven voltage with the magnitude of 100 V was used to actuate the piezoelectric stacks. Then the voltage dropped to 0 V suddenly to provide the instantaneous driven force. Notably, back pressure for the syringe was 250 kPa to force the ink into the chamber. The frequency was 120 Hz, and the moving velocity of printing head was 20 mm/s. Temperature was maintained at 25 °C, while humidity was 60% for lab environment.

Characterization

To closely observe the quality of micro patterns, surface morphologies of the millirobot and microconical matrix were characterized by field emission scanning electron microscope (SEM, Scios, Thermo fisher) and super deep scene microscope (VHX-2000, Keyence, Japan). The height and 3D morphology of the microconical matrix were measured by step profiler (Dektak XT, BRUKER, Germany). Strain rate was set to be at a rate of 15 mm/min. The millirobot locomotion, jet printing process and magnetization-induction process were record by high-speed camera (M230M, Revealer AgileDevice). Rheological responses of the composite inks were characterized by a rheometer (Anton Paar MCR 92). Ink viscosity was tested with shear rate ranging from 0.1 to $100\,\text{s}^{-1}$.

Electrical measurement

For electrical measurement of the sensing module, an Ag layer was prepared as the positive electrode, while an ITO electrode underneath was set as the negative electrode. Microconical matrix is constructed on ITO electrode as the dielectric charging layer. To study the electrical characteristics of the sensing module in vertical contact-separation mode, the two electrodes were fixed on acrylic glass and positioned face to face. A home-made testing platform equipped with a linear motor was employed to secure all electrodes of the sensor. The contact frequency (ranging from 1 Hz to 4 Hz) and distance during the periodical contact/septation could be controlled by the linear motor. In bending mode, the sensing module was attached on a PET film, and a moving stage was used to fix the two edges of the PET film. By accurately controlling the distance between these two edges, the curvature of the sensing module could be adjusted correspondingly. For electrical measurement, the open-circuit voltage was measured by high-impedance electrometer (Model 6514, Keithley) and data acquisition card (USB 6349, National instruments). The acquired data were recorded via customized LabView program. The contact force was monitored with the force sensor (M3552C, Sunrise Instruments, China).

Environment awareness based on machine learning

Extracting features directly and quickly from the signals, particularly those that are similar, posed a significant challenging. Thus, we introduced a neural network architecture named Temporal Perceiver Network, which could automatically learn, extract, and classify features from the data. In detail, Fast Fourier Transform (FFT) was applied to data by transforming time series into frequency domain. Subsequently, the Top K values within the highest amplitude in the frequency domain were selected to divide and split the corresponded data in time series. Then, the time segments were stacked into a two-dimensional time signal. This data processing method aimed to capture variations both within each time segment and between different segments. Subsequently, multi-scale convolution blocks were used to extract features of the data.

As for data collection, five different terrain surfaces were prepared for environmental recognition, including sandpaper, wood, plastic, 3D printed PLA plate, and paper. Output voltage signals in time-series were produced and recorded by the millirobot. Data were collected, of which 80% sets were for training, 20% sets were for testing. We employed a sliding window method to select training samples, where the window size was set to 25 data points and the step size was 15 data points.

Data availability

No datasets were generated or analysed during the current study.

References

1. Lin, Y. et al. A bioinspired stress-response strategy for high-speed soft grippers. *Adv. Sci.* **8**, 2102539 (2021).
2. Eshaghi, M., Ghasemi, M. & Khorshidi, K. Design, manufacturing and applications of small-scale magnetic soft robots. *Extrem. Mech. Lett.* **44**, 101268 (2021).
3. Shintake, J., Cacucciolo, V., Floreano, D. & Shea, H. Soft robotic grippers. *Adv. Mater.* **30**, 1707035 (2018).
4. Cacucciolo, V. et al. Stretchable pumps for soft machines. *Nature* **572**, 516–519 (2019).
5. Lai, Y. C. et al. Actively perceiving and responsive soft robots enabled by self-powered, highly extensible, and highly sensitive triboelectric proximity-and pressure-sensing skins. *Adv. Mater.* **30**, 1801114 (2018).
6. Kim, Y. et al. Telerobotic neurovascular interventions with magnetic manipulation. *Sci. Robot.* **7**, eabg9907 (2022).
7. Niu, H. et al. Magworm: a biomimetic magnet embedded worm-like soft robot. *Soft Robot.* **8**, 507–518 (2021).
8. Hu, W., Lum, G. Z., Mastrangeli, M. & Sitti, M. Small-scale soft-bodied robot with multimodal locomotion. *Nature* **554**, 81–85 (2018).

9. Lee, J.-Y. et al. Shape-adaptive universal soft parallel gripper for delicate grasping using a stiffness-variable composite structure. *IEEE Trans. Ind. Electron.* **68**, 12441–12451 (2020).

10. Tang, C. et al. A pipeline inspection robot for navigating tubular environments in the sub-centimeter scale. *Sci. Robot.* **7**, eabm8597 (2022).

11. Ren, Z. et al. Soft-bodied adaptive multimodal locomotion strategies in fluid-filled confined spaces. *Sci. Adv.* **7**, eabh2022 (2021).

12. Liang, J. et al. Electrostatic footpads enable agile insect-scale soft robots with trajectory control. *Sci. Robot.* **6**, eabe7906 (2021).

13. Liu, Y. et al. Bioinspired triboelectric soft robot driven by mechanical energy. *Adv. Funct. Mater.* **31**, 2104770 (2021).

14. Zhou, W. & Li, Y. Modeling and analysis of soft pneumatic actuator with symmetrical chambers used for bionic robotic fish. *Soft Robot.* **7**, 168–178 (2020).

15. Terryn, S., Brancart, J., Lefeber, D., Van Assche, G. & Vanderborght, B. Self-healing soft pneumatic robots. *Sci. Robot.* **2**, eaan4268 (2017).

16. Wu, S., Hong, Y., Zhao, Y., Yin, J. & Zhu, Y. Caterpillar-inspired soft crawling robot with distributed programmable thermal actuation. *Sci. Adv.* **9**, eadf8014 (2023).

17. Wu, S., Baker, G. L., Yin, J. & Zhu, Y. Fast thermal actuators for soft robotics. *Soft Robot.* **9**, 1031–1039 (2022).

18. Xiao, Y.-Y., Jiang, Z.-C. & Zhao, Y. Liquid crystal polymer-based soft robots. *Adv. Intell. Syst.* **2**, 2000148 (2020).

19. Lv, P. et al. Stimulus-driven liquid metal and liquid crystal network actuators for programmable soft robotics. *Mater. Horiz.* **8**, 2475–2484 (2021).

20. Venkiteswaran, V. K., Samaniego, L. F. P., Sikorski, J. & Misra, S. Bio-inspired terrestrial motion of magnetic soft millirobots. *IEEE Robot. Autom. Lett.* **4**, 1753–1759 (2019).

21. Dong, Y. et al. Untethered small-scale magnetic soft robot with programmable magnetization and integrated multifunctional modules. *Sci. Adv.* **8**, eabn8932 (2022).

22. Wang, L. et al. Evolutionary design of magnetic soft continuum robots. *Proc. Natl. Acad. Sci.* **118**, e2021922118 (2021).

23. Kim, Y., Parada, G. A., Liu, S. & Zhao, X. Ferromagnetic soft continuum robots. *Sci. Robot.* **4**, eaax7329 (2019).

24. Son, D., Ugurlu, M. C. & Sitti, M. Permanent magnet array–driven navigation of wireless millirobots inside soft tissues. *Sci. Adv.* **7**, eabi8932 (2021).

25. Yang, X. et al. An agglutinate magnetic spray transforms inanimate objects into millirobots for biomedical applications. *Sci. Robot.* **5**, eabc8191 (2020).

26. Yang, X., Tan, R., Lu, H. & Shen, Y. Starfish inspired milli soft robot with omnidirectional adaptive locomotion ability. *IEEE Robot. Autom. Lett.* **6**, 3325–3332 (2021).

27. Sun, D. et al. Analysis and control for a bioinspired multi-legged soft robot. *Biomim. Intell. Robot.* **2**, 100030 (2022).

28. Lu, H. et al. A bioinspired multilegged soft millirobot that functions in both dry and wet conditions. *Nat. Commun.* **9**, 3944 (2018).

29. Tan, R. et al. Nanofiber-based biodegradable millirobot with controllable anchoring and adaptive stepwise release functions. *Matter* **5**, 1277–1295 (2022).

30. Li, G., Zhang, T. & Shen, Y. Transparent magnetic soft millirobot actuated by micro-node array. *Adv. Mater. Technol.* **6**, 2100131 (2021).

31. Gu, H. et al. Magnetic cilia carpets with programmable metachronal waves. *Nat. Commun.* **11**, 2637 (2020).

32. Rafsanjani, A., Zhang, Y., Liu, B., Rubinstein, S. M. & Bertoldi, K. Kirigami skins make a simple soft actuator crawl. *Sci. Robot.* **3**, eaar7555 (2018).

33. Yang, X., Chang, L. & Pérez-Arancibia, N. O. An 88-milligram insect-scale autonomous crawling robot driven by a catalytic artificial muscle. *Sci. Robot.* **5**, eaba0015 (2020).

34. Wu, Y. et al. Insect-scale fast moving and ultrarobust soft robot. *Sci. Robot.* **4**, eaax1594 (2019).

35. Chen, R. et al. Legless soft robots capable of rapid, continuous, and steered jumping. *Nat. Commun.* **12**, 7028 (2021).

36. Kim, T. et al. Ultra-stable and tough bioinspired crack-based tactile sensor for small legged robots. *npj Flex. Electron.* **7**, 22 (2023).

37. Wang, H. et al. Magnetic soft robots: design, actuation, and function. *J. Alloy. Compd.* **922**, 166219 (2022).

38. Ju, Y. et al. Reconfigurable magnetic soft robots with multimodal locomotion. *Nano Energy* **87**, 106169 (2021).

39. Li, H. et al. 3D printed flexible triboelectric nanogenerator with viscoelastic inks for mechanical energy harvesting. *Nano Energy* **58**, 447–454 (2019).

40. Li, X. et al. Limpet tooth-inspired painless microneedles fabricated by magnetic field-assisted 3D printing. *Adv. Funct. Mater.* **31**, 2003725 (2021).

41. Seol, M. L. et al. All-printed triboelectric nanogenerator. *Nano Energy* **44**, 82–88 (2018).

42. Li, H. et al. Wearable triboelectric nanogenerator with micro-topping structures via material jet printing method. *Nano Energy*, 108650 (2023).

43. Qu, X. et al. Artificial tactile perception smart finger for material identification based on triboelectric sensing. *Sci. Adv.* **8**, eabq2521 (2022).

44. Peng, X. et al. A breathable, biodegradable, antibacterial, and self-powered electronic skin based on all-nanofiber triboelectric nanogenerators. *Sci. Adv.* **6**, eaba9624 (2020).

Acknowledgements

Author contributions

W.Z. and X.D. conceived and planned the experiments and sample preparation, Y.J., B.L. contributed to measurements and formal analysis, R.Z. and H.L. wrote original draft, F.G., Y.L. and L.J. reviewed and edited the manuscript, L.J. supported experiments and data preparation, H.L. conceived the research concept, secured funding, and supervised the project, providing guidance throughout its development and ensuring its successful completion. All authors helped shape the research and revise the manuscript.

Competing interests

The authors declare no competing interests.

Additional information

Supplementary information The online version contains supplementary material available at https://doi.org/10.1038/s41528-025-00437-0.

Correspondence and requests for materials should be addressed to Runhao Zeng, Lelun Jiang or Hui Li.

Reprints and permissions information is available at http://www.nature.com/reprints